IOP Publishing Journal of Physics D: Applied Physics
J. Phys. D: Appl. Phys. **40** (2007) 2603–2612 doi:10.1088/0022-3727/40/8/027

A collision model for a large number of particles with significantly different sizes

N Zhang and Z C Zheng[1]

Department of Mechanical and Nuclear Engineering, Kansas State University, Manhattan, KS 66506-5205, USA

E-mail: zzheng@ksu.edu

Received 10 August 2006, in final form 9 February 2007
Published 4 April 2007
Online at stacks.iop.org/JPhysD/40/2603

Abstract
A collision model, modified from the Smoluchowski model, is developed for simulating coagulation and growth of a large number of aerosol particles with significantly different sizes. In this collision model, the particle-size distribution is discretized in volume bins, and the total mass among all the bins is conserved. In situations with significantly different particle sizes, the present model reduces the number of bins compared with the previous models, thus reducing the computational cost. By comparing the results of the present model with the exact solution of Smoluchowski's original model, the accuracy of the solution is not sacrificed. Therefore, this model enables the real-time simulation of three-dimensional, two-phase flow when flow/particle interactions need to be considered. After implementation with a flow solver, the model is further validated with the data from a smoke-reduction experiment in a room-scale chamber using flow-injected nanoparticle aggregates.

1. Introduction

Aerosol coagulation is one of the major phenomena that affect the composition and size distribution of particles. For a homogeneous system, the population balance for the evolution of the particle-number density of Size i particles, n_i, was defined by Smoluchowski (1917):

$$\frac{\mathrm{d}n_i}{\mathrm{d}t} = \frac{1}{2}\sum_{j=1}^{i-1} K_{i-j,j} n_{i-j} n_j - n_i \sum_{j=1}^{\infty} K_{i,j} n_j \ , \qquad (1)$$

where $K_{i,j}$ is the collision kernel for collisions between Size i and Size j particles. Note that the volume of a Size i particle is i times the volume of a particle of Size 1. The first term on the right-hand side of equation (1) accounts for the increase in Size i particles due to collisions of smaller sized particles, and the second term accounts for the losses from this size of particles due to collisions with particles of other sizes.

In practical applications, to cover the size range from smallest to largest, millions of different sized particles are needed, and equation (1) needs to be solved as many times. For example, if the particle diameter ranges from 1 to 100 μm, then at least 1 million sizes are needed, because the sizes of particles are determined by

$$d_i = i^{1/3} d_1 \ , \qquad (2)$$

where d_i is the diameter of a Size i particle. Thus the computational cost is prohibitively high for a problem in a three-dimensional domain. Although some successful implementations of the above equation have been reported (e.g. Reade and Collins 2000), most of them are implemented on a single grid. In unsteady, three-dimensional flow problems, the number of computational grids is at least thousands, or even millions. It is thus nearly impossible to solve equation (1) for particles of all sizes on every computational grid at each time step. Therefore, approximating a virtually continuous size spectrum using a set of size classes, or bins, is very much needed in reality. In an early simulation by Lawler *et al* (1980), a weighting function is introduced to distribute coagulated particles whose sizes are between two consequent bins into each of these two bins. There are other approaches using this discrete bin structure including those of Gelbard *et al* (1980), Batterham *et al* (1981), Marchal *et al* (1988) and Hounslow *et al* (1988). In the review work of Kostoglou and Karabelas (1994), the authors compare these four approaches and refer

[1] Author to whom any correspondence should be addressed.

to this type of coagulation methods as 'zero order methods,' when the distribution within each bin is assumed to be constant. They also stated that the zero order methods usually result in diffusion errors while the higher order methods reduce the diffusion errors but tend to introduce dispersion errors. There are more recent zero order methods implemented by Jacobson *et al* (1994) and Sandu (2002) and higher order methods by Fernandez-Diaz *et al* (2000). In these three implementations, it is assumed that the particle-number density inside one volume bin is uniform and the volume ratio of two adjacent bins has to be small enough (<1.5) to provide accurate results.

The method developed in this study is designed for simulating practical gas/particle multiphase flow problems. The first targeted issue that leads to the development of the model is related to coupled simulation between flow and particles on a large number of three-dimensional computational grids, with turbulence present. For this type of problem, the simulation of flow phase is already expensive. For the particulate phase, the number of equations is determined by the number of bins. It is therefore necessary to reduce the bin number to the minimum, i.e. to increase the volume ratio of two adjacent bins to the maximum. For this purpose, several modifications and approximations have been made to equation (1). In the current method, larger sizes of bins can be used without losing desired accuracy. The second issue for having this model is related to the collision simulation for particles with significantly different sizes. For example, by using nanoparticle aggregates to reduce smoke in a chamber, relatively large particles are injected into a chamber to 'capture' very small smoke particles. For this problem, since the size difference is so big between the nano-aggregates and smoke particles, the effect of collision between same sized particles is negligible compared with the collisions between different sized particles. The continuous bin structures between the small and large particles are very wasteful in this problem. The current method uses the discontinuous bin structures, thus reducing the computational cost significantly.

There are several advantages of the current model over the previous methods. In the literature, most of the collision models have been developed for specific purposes, such as pelletization (Batterham *et al* 1981), crystallization (Marchal *et al* 1988, Hounslow *et al* 1988) and aerosols (Gelbard *et al* 1980). Although the intended applications of the current model are closely related to the behaviour of aerosols, the computational difficulties related to the double integrals in Gelbard *et al* (1980)'s method negate the overall computational benefits of using their approach, as pointed out by Kostoglou and Karabelas (1994). For the nature of the smoke-reduction application, the number of different particle sizes involved is small, while the three-dimensional flow computation is rather heavy. The current collision model is thus designed for handling this particular computational need. Using the current model, the size spectrum can be minimized into the smallest number of bins in comparison to other methods, maintaining a reasonably achievable accuracy. The possible errors, which are rooted in enforcing conservation of mass rather than conservation of particle numbers, can be controlled to a minimal level when the mass ratio between the small and large particles is very small in the application. Therefore the current model enables a practical implementation of the unsteady three-dimensional simulation of two-phase flow problems with flow/particle interactions.

2. Description of the present collision model

While equation (1) represents a population balance in terms of particle numbers, the basic assumption adopted in the present coagulation method is that the total mass of all the bins is conserved. All the particles considered are assumed spherical. When the collisions occur, the mass lost in certain sizes of particles is equal to the mass increase in the other sizes of particles. This mass balance can be written as

$$\frac{\mathrm{d}\rho_i}{\mathrm{d}t} = \sum_{j=1}^{i-1} \Delta\rho_{j \text{ loss to } i} - \sum_{j=1}^{\infty} \Delta\rho_{i \text{ loss to } j}, \tag{3}$$

where ρ_i is the mass of the Size i particles, and is defined as

$$\rho_i = w_i n_i = \frac{1}{6}\pi d_i^3 \gamma_i n_i, \tag{4}$$

where w_i (kg/count) and γ_i are the weight of an individual particle and material density of Size i particles, respectively. Equation (3) represents the change of mass with time for Size i particles. The first term on the right-hand side of equation (3) is the mass gain due to collisions of smaller sized particles, while the second term accounts for the mass loss of the current sized particles due to collisions between the current size and the other sizes. The mass loss in one size is accounted for by the mass increase in the other sizes. The expression for $\Delta\rho_{j \text{ loss to } i}$ will be determined in section 2.1.

Now if we consider mass balance among volume bins instead of among particle sizes, equation (3) still stands, with the index i now denoting Bin i instead of Size i, and ρ_i represents the mass of Bin i. At this point, an additional variable needs to be introduced, the volume ratio between two bins:

$$V_{i,j} = \frac{v_i}{v_j} = \frac{\mathrm{d}_i^3}{\mathrm{d}_j^3}, \tag{5}$$

where v_i is the volume of particles in Bin i. If $V_{i,j}$ is constant between two consecutive bins, by denoting this ratio as V_{ratio}, we have

$$V_{\text{ratio}} = \frac{v_{i+1}}{v_i}. \tag{6}$$

For any values of V_{ratio} greater than one, the volume of a Bin i particle is

$$v_i = v_1 V_{\text{ratio}}^{i-1} \tag{7}$$

and its radius is

$$r_i = r_1 V_{\text{ratio}}^{(i-1)/3}. \tag{8}$$

Consequently, from equation (8), it can be deduced that the number of bins that covers the particle-size range from radius r_1 to r_i is

$$i = 1 + \ln[(r_i/r_1)^3]/\ln[V_{\text{ratio}}]. \tag{9}$$

In realistic applications, the ratios between two consecutive bins may not always be constant.

Under the bin structures, there exist two scenarios of particle collisions: (1) collisions between two different bins and (2) collisions within one bin. Each of these two scenarios are dealt with, respectively, in the next two subsections.

2.1. Collisions between two different bins (inter-bin collisions)

If V_{ratio} is large, the two adjacent bins have a wide size difference. Therefore, when collisions occur between a certain bin of small particles (small bin) and a certain bin of large particles (large bin), we assume that the resulting particles will fall only into that particular large bin and not into any other larger bin. That is, the mass loss from the small bin equals the mass increase in the large bin. When this type of collisions happen, the mass loss in a bin is incurred only when the particles in this bin collide with particles in larger bins. The mass loss in Bin j is based on equation (1):

$$\Delta\rho_{j\ \text{loss to}\ i} = w_j \Delta n_{j\ \text{loss to}\ i} = w_j K_{i,j} n_i n_j. \tag{10}$$

Hence, the addition in Bin i is

$$\sum_{j=1}^{i-1} \Delta\rho_{j\ \text{loss to}\ i} = \sum_{j=1}^{i-1} w_j K_{i,j} n_i n_j. \tag{11}$$

The summation in equation (11) corresponds to the overall gain in Bin i due to collisions with all the smaller bins. Based on the definition of w_i in equations (4) and (5), we can get

$$w_j = V_{j,i} w_i \frac{\gamma_j}{\gamma_i} = \frac{w_i}{V_{i,j}} \frac{\gamma_j}{\gamma_i}. \tag{12}$$

Hence, equation (11) becomes

$$\sum_{j=1}^{i-1} \Delta\rho_{j\ \text{loss to}\ i} = \sum_{j=1}^{i-1} \frac{\gamma_j}{\gamma_i V_{i,j}} w_i K_{i,j} n_i n_j. \tag{13}$$

On the other hand, the mass loss in Bin i, which is due to collisions only between Bin i particles and particles in the bins larger than Bin i, can be expressed using equation (10) as

$$\sum_{j=i+1}^{\infty} \Delta\rho_{i\ \text{loss to}\ j} = \sum_{j=i+1}^{\infty} w_i \Delta n_{i\ \text{loss to}\ j} = \sum_{j=i+1}^{\infty} w_i K_{j,i} n_j n_i. \tag{14}$$

Note the summation in the above equation starts at $i + 1$, indicating that the mass loss is caused only by collisions happening between the current bin and the larger bins. Substituting equations (11) and (14) into equation (3), we have

$$\frac{\mathrm{d}\rho_i}{\mathrm{d}t} = \frac{\mathrm{d}(w_i n_i)}{\mathrm{d}t} = \sum_{j=1}^{i-1} \frac{\gamma_j}{\gamma_i V_{i,j}} w_i K_{i,j} n_i n_j - \sum_{j=i+1}^{\infty} w_i K_{j,i} n_j n_i. \tag{15}$$

We also assume that w_i does not change with time, dividing w_i from both sides of equation (15) to yield, in terms of particle-number density,

$$\frac{\mathrm{d}n_i}{\mathrm{d}t} = n_i \sum_{j=1}^{i-1} \frac{\gamma_j}{\gamma_i V_{i,j}} K_{i,j} n_j - n_i \sum_{j=i+1}^{\infty} K_{i,j} n_j. \tag{16}$$

The first term on the right-hand side of equation (16) accounts for the addition from the smaller bin particles colliding with the current bin particles, while the second term accounts for the loss of the current bin particles colliding with the particles in larger bins. This equation is based on the assumption that all collisions within one bin can be neglected. In other words, collisions among particles within the same bin would not generate particles large enough to jump into the next larger bin. Under this assumption, although the number or the average size of the particles in this bin may change due to the inner-bin collision, the total mass of this bin still remains the same if there are only inner-bin collisions.

It needs to be mentioned that in equation (16), mass conservation is represented in terms of particle-number densities. The particle volumes before and after inter-bin collisions are not conserved at the same time. Since the size and material density of particles in each bin are assumed unchanged when inter-bin collisions occur, the particle-number density in the large bin has to change to enforce the mass conservation. This contradicts the reality where the size and material density of the resultant particle can change instead. However, the model is intended to reasonably predict particle-number densities by enforcing mass conservation, because the capture efficiency in particle collisions is proportional to the time-dependent number densities of the particles.

It is noticed that equation (16) can be re-written as

$$n_i(t) = n_i(0) \exp\left[\int_0^t \left(\sum_{j=1}^{i-1} \frac{\gamma_j}{\gamma_i V_{i,j}} K_{i,j} n_j - \sum_{j=i+1}^{\infty} K_{i,j} n_j\right) \mathrm{d}t\right], \tag{17}$$

where the value of n_i remains zero if initially n_i at $t = 0$ is zero. As stated at the beginning of this subsection, when the small-bin j and large-bin i particles collide, this model allows the reactant particles, i-bin and j-bin particles, to become i-bin particles only. The errors due to this assumption become negligible in most of our applications in which the growth rate of n_i, represented by the exponential function in equation (17), is not excessively large. Again, this inter-bin model only works well in those applications where the differences in particle sizes are very big and the bins are discontinuous, such as in the smoke-reduction application, when very large particles are injected to capture very small smokeparticles. The results of the smoke-reduction application will be presented in the next section.

A validation case has been facilitated to compare the results from equations (16) and (1). The result using equation (1) is considered the 'exact' solution. The case is for two groups of significantly different sizes of particles, with initially mono-sized particles in each group. The particles are confined in a cube of 1 m^3 that has no mass in and no mass out, so that the total mass is conserved. There are a total of 550 consecutive sizes to be included in the exact simulation, from Size 1 to Size 550. At the beginning of the simulation, the nonzero-number particles, with substantially different sizes as the intended model case, are selected, Size 1 and Size 64. All the other sizes are initially with zero particle number. The particles are of the same material so that the material density is the same for different sized particles. The initial particle-number densities are specified as $n_{\text{size1}} = 1 \times 10^{12} \text{count m}^{-3}$ and $n_{\text{size64}} = 1.5625 \times 10^{10}$ count m^{-3}, and zero for the other sizes. The reason for selecting the value of n_{size64} is to match the same mass as Size 1. The physical diameter of Size 1 particles is specified as 1 μm so that the physical diameter of Size 64 particles is 4 μm, according to equation (2).

When applying the present model for simulation to compare with the above described exact simulation, three bins are used. Bin 1 to include Sizes 1–7 particles, Bin 2 to include Sizes 8–63 and Bin 3 to include Sizes 64–511. The initial particle-number density in each of the bins becomes

$$n_{\text{bin1}} = \sum_{i=1}^{7} n_{\text{size}_i}, \tag{18}$$

$$n_{\text{bin2}} = \sum_{i=8}^{63} n_{\text{size}_i} \tag{19}$$

and

$$n_{\text{bin3}} = \sum_{i=64}^{511} n_{\text{size}_i}. \tag{20}$$

Therefore, from the initial condition for the exact simulation, the corresponding initial condition for the bin model becomes $n_{\text{bin1}} = n_{\text{size1}}$, $n_{\text{bin2}} = 0$ and $n_{\text{bin3}} = n_{\text{size64}}$. Note that in the exact equation, equation (1), the particle-number density is for each size, while in the bin model, equation (16), the particle-number density is for each bin. A constant volume ratio between the two consecutive bins, $V_{\text{ratio}} = 8$, is used. The representative diameters of the particles in each of the bins are 1 μm, 2 μm and 4 μm, respectively.

A homogeneous, isotropic, constant-intensity turbulence is specified as the background turbulence for the collision mechanism. The Saffman–Turner collision kernel (1956) is used in the simulation as

$$K_{(\text{turb})i,j} = \left(\frac{8\pi}{15}\right)^{1/2} \frac{a_{i,j}^3}{t_k}, \tag{21}$$

where $a_{i,j}$ is the collision diameter defined as $r_i + r_j$ and t_k is the Kolmogorov time scale defined as $(\nu/\epsilon)^{1/2}$ with ν and ϵ, respectively, the kinematic viscosity and the turbulence dissipation rate. In this test case, a relatively strong turbulence level is specified, resulting in the constant part of equation (21) becoming

$$\left(\frac{8\pi}{15}\right)^{1/2} \frac{1}{t_k} = 1000(1/\text{s})\ . \tag{22}$$

The total simulated time is one minute and the time step is 0.05 s. A first-order Euler scheme is used for time marching. This scheme is selected for its simplicity of coding and easy implementation later with the fluid flow solver. The accuracy of the selected time step has been tested by comparing the results using a time step of 0.1 s and showing negligible differences. Figure 1 shows the evolution histories of the mass of each bin. The ordinate in figure 1 is the volume fraction of each bin's particles in the cube. Because all the particles are of the same material, the volume fraction can be used as indicative of mass balance among the bins. Since the results of the exact solution are for each size, for the purpose of comparison, we combine the total mass in Size 1–Size 7 to represent the mass of Bin 1, Size 8–Size 63 for Bin 2 and Size 64–Size 511 for Bin 3. It is clear that the present model matches the exact solution perfectly. The mass of Bin 1 decreases while the mass of Bin 3 increases, justifying the assumption that the collisions between the small-bin particles and the large-bin particles lead to the resulting particles falling into the large bin. According

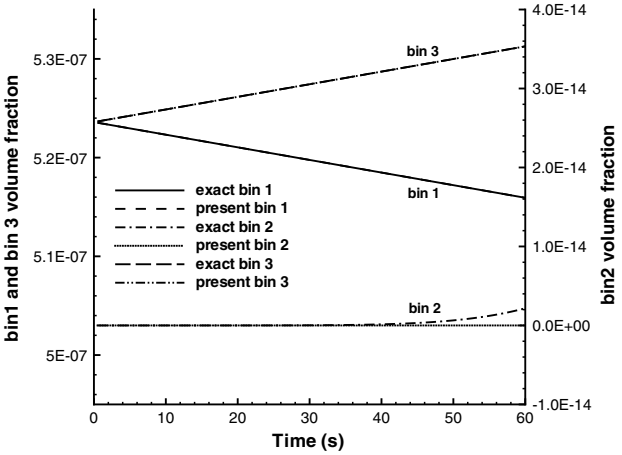

Figure 1. Time history comparison of total mass in each bin between the present model and the exact solution.

to the wide-bin-width assumption in the present model, since the particle-number density of Bin 2 is originally zero, it would remain zero in this bin all the time in the results of this model, as expressed in equation (17). It is also evident from the results of the exact simulation that the value of particle-number density in Bin 2 is very small (close to zero), with the value of particle-number density approximately 8 orders of magnitude smaller than those in the other bins even after a minute of simulation time. That means that the inner-bin collisions in Bin 1 are unlikely to generate particles large enough to jump into the next bin if the bin width is sufficient.

Another aspect to be pointed out is the shape effect of the particles on the population dynamics. Kostoglou *et al* (2006) used a fractal dimension, D, to define the morphology of aggregates:

$$m = k\left(\frac{R}{\alpha}\right)^D, \tag{23}$$

where R is the radius of the aggregate consisting of m smaller primary spherules of size α and k is a constant. The fractal dimension, D, varies from 1 (linear addition) to 3 (complete coalescence). In that study, the parametric evolution of the fractal dimension of aggregates was thus developed, and the case of Brownian coagulation in the continuum regime was studied. They stated that the fractal dimension of a small aggregate colliding with a large aggregate has small influence on the fractal dimension of the resulting aggregate. This is the same situation as in the current simulation where small bin particles collide with large bin particles. Therefore, the variation of the fractal dimension of the large bin particles is negligible. In equation (5), it is shown that the fractal dimension in the current model is fixed at 3. However, other fractal dimensions can possibly be included if more detailed models of physical processes need to be considered such as the structure of aggregates. In addition, mass conservation is the first priority in the current model, as shown in equation (3), the starting equation of the model. The volume is then determined based on the fixed material density of each bin, assuming the change of material density is negligible. If the material density of each bin is the same, then the overall volume of particles is conserved simultaneously. If not, the volume is not conserved. In that sense, the variation of fractal dimension is

not as important as in the approaches by Kostoglou *et al* (2006) where the volume of the resulting aggregate is determined by the fractal dimension.

2.2. Collisions within one bin (inner-bin collisions)

When the bin width is not very large, inner-bin collisions can produce particles that belong to the bins of larger particles. In this model, we only consider the case that the inner-bin collisions cause particles to jump into the immediate-next larger bin, but not into other larger bins. That is, when Bin i particles collide with each other, a portion of the resulting particles can become the particles in the larger bin, Bin $i+1$. To account for this effect, two more terms are added to equation (16):

$$\frac{\mathrm{d}n_i}{\mathrm{d}t} = \sum_{j=1}^{i-1} \frac{\gamma_j}{\gamma_i V_{i,j}} K_{i,j} n_i n_j + \frac{\gamma_{i-1}}{\gamma_i V_{i,i-1}} C_{i-1} K_{i-1,i-1} n_{i-1} n_{i-1} - n_i \sum_{j=i+1}^{\infty} K_{i,j} n_j - C_i K_{i,i} n_i n_i, \tag{24}$$

where all the constants C_i vary from 0 to 1, representing the probability of the resulting particles that can jump into the next bin. The second and the fourth terms on the right-hand side of equation (24) are the added terms accounting for the addition and loss from the inner-bin collisions. If all the C_i are very small or if the collision kernel, K, between two same sized particles is very small, the second and the fourth terms can be neglected. Under these conditions, equation (24) reduces to equation (16).

In the current volume-bin model, the size of particles in a bin is always assumed at the lowest end of the bin. The generality of the method is not lost with this assumption because of the fact that the volume ratio, as defined in equation (5), need not be constant. The inner-bin-collision effect in different bin sizes should then be included in the values of the inner-bin-collision coefficient C_i. Obviously, this coefficient varies with different bin ratios. For example, in the previous validation case in section 2.1, the bin-volume ratio is 8, and the inner-bin collision is very insignificant according to the exact simulation of equation (1). Based on the assumption of this model, if the bin-volume ratio is 2, all the C_i values are 1 in all the bins because any inner-bin collision can result in a particle in the next bin.

In order to test the bin-ratio effect on the value of C, we use numerical experiments to investigate the behaviour of C. While it is difficult, if not impossible, to simultaneously determine all the C_i values that can also change with time, we design the numerical experiment to target the first C value C_1, after one minute of simulation time. In the numerical experiments, for the exact simulation, Size 1 particles of 1 μm diameter are initially assigned a particle-number density of $n_{\mathrm{size1}} = 1\times10^{12}$ count m^{-3} for the '1×' case, with all the other sizes of particles having a zero particle-number density. As a result, in the present bin-model simulation, the initial condition for particle-number density in each bin is $n_{\mathrm{bin1}} = n_{\mathrm{size1}}$, and $n_{\mathrm{bini}} = 0$ for the rest of the bins. The cases of '2×,' '5×' and '10×' are also tested to investigate the effect of initial particle-number density, with the initial particle-number density being twice, five times and ten times, respectively, that of the value in the '1×' case.

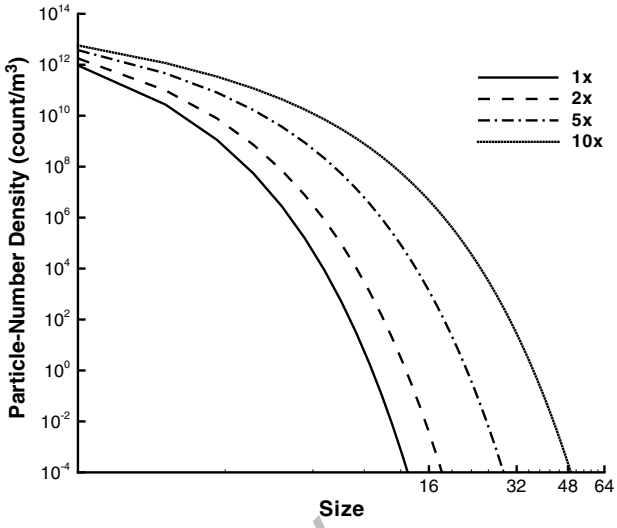

Figure 2. Distribution of particle-number density versus particle size from the exact solution using Smoluchowski's model, equation (1), for the cases of '1×,' '2×,' '5×' and '10×.'

The total number of consecutive sizes included in the exact solution, the computation of equation (1), is again 550. The distribution of particle-number density after one minute of exact simulation for the first 64 sizes is plotted in figure 2. The first three columns in table 1 show the particle-number density of the exact solution after the one-minute simulation, grouped into each bin with the bin ratio from 2 to 8 at the four different initial particle-number density values for Size 1 particles (the '1×,' '2×,' '5×' and '10×' cases).

For the first three bins in the bin-model simulation, each is assigned a C value, C_1, C_2 and C_3, respectively. The fourth column in table 1 represents the C value in Bin 1, C_1, using the exact simulation results after one-minute simulation. A guessed value of C_1 is initially put into equation (24) for a certain bin ratio, with C_2 and C_3 assigned zero. Then the calculated result using these C values is compared with the particle-number density of Bin 1 and Bin 2 from the exact solution of equation (1) after one minute of simulation. With several times of calibrations of C_1, the two results match exactly. The resulting C_1 value is thus considered a correct value to represent the inner-bin collision for that particular bin ratio and particular initial particle-number density. Note that with the assumption of a zero value of C_2 and C_3, the determined C_1 value is only valid when the particle-number density of the exact solution in Bin 3 is sufficiently small, which indicates the inner-bin collision in Bin 2 is negligible, thus justifying the usage of $C_2 = 0$ and $C_3 = 0$. This is because with C_2 and C_3 being zero, from the bin-model equation, equation (24), the inner-collision terms (the second and fourth terms) are also zero, equivalent to the inter-collision only case for Bin 3. And with $n_{\mathrm{bin3}} = 0$ initially, the two inter-collision terms (the first and third terms) are zero, too. As a result, n_{bin3} remains zero in the bin model. Therefore, the C_1 values in table 1 are only listed for the cases when the particle-number density of the exact solution in Bin 3 is less than $<10^{-5}$ times those of Bin 1 and Bin 2. In this sense, the inner-bin

Table 1. Particle-number density values in each bin and the model C_1 values at different volume ratios in the cases of (*a*) '1×,' (*b*) '2×,' (*c*) '5×' and (*d*) '10×.'

Volume ratio	Bin 1	Bin 2	Bin 3	*C*
(*a*) 1×				
2	9.422 32E+11	5.753 67E+10	2.317 99E+08	1.00000E+00
3	9.963 97E+11	3.602 72E+09	2.987 09E+02	5.917 29E−01
4	9.997 68E+11	2.318 04E+08	2.000 00E-06	3.801 93E−03
5	9.999 85E+11	1.516 32E+07	0.000 00E+00	2.489 73E−04
6	9.999 99E+11	1.001 92E+06	0.000 00E+00	1.646 67E−05
7	1.000 00E+12	6.664 58E+04	0.000 00E+00	1.096 13E−06
8	1.000 00E+12	4.454 08E+03	0.000 00E+00	7.329 98E−08
(*b*) 2×				
2	1.777 33E+12	2.193 58E+11	3.306 58E+09	1.000 00E+00
3	1.973 28E+12	2.672 29E+y10	1.121 76E+05	1.087 98E−01
4	1.996 69E+12	3.307 45E+09	7.013 40E-02	1.336 08E−02
5	1.999 58E+12	4.161 29E+08	0.000 00E+00	1.683 02E−03
6	1.999 95E+12	5.288 31E+07	0.000 00E+00	2.142 56E−04
7	1.999 99E+12	6.765 61E+06	0.000 00E+00	2.745 08E−05
8	2.000 00E+12	8.696 54E+05	0.000 00E+00	3.532 69E−06
(*c*) 5×				
2	3.748 89E+12	1.158 17E+12	9.233 28E+10	1.000 00E+00
3	4.664 00E+12	3.358 25E+11	1.752 57E+08	
4	4.907 06E+12	9.294 11E+10	3.043 05E+04	5.815 20E−02
5	4.973 88E+12	2.612 22E+10	4.703 50E-01	1.623 34E−02
6	4.992 59E+12	7.414 84E+09	1.000 00E-06	4.613 04E−03
7	4.997 88E+12	2.118 74E+09	0.000 00E+00	1.321 68E−03
8	4.999 39E+12	6.082 91E+08	0.000 00E+00	3.804 74E−04
(*d*) 10×				
2	5.748 37E+12	3.354 42E+12	8.502 73E+11	1.000 00E+00
3	8.073 36E+12	1.903 91E+12	2.272 96E+10	
4	9.102 80E+12	8.970 54E+11	1.498 71E+08	
5	9.575 84E+12	4.241 56E+11	2.494 01E+05	6.336 36E−02
6	9.797 57E+12	2.024 34E+11	1.032 57E+02	2.985 26E−02
7	9.902 76E+12	9.724 22E+10	1.055 50E-02	1.429 66E−02
8	9.953 07E+12	4.693 09E+10	0.000 00E+00	6.906 85E−03

collision considered in the numerical experiments is based on the mass conservation between Bin 1 and Bin 2 only. In all the numerical experiments, the collision mechanism is generated using the same turbulence background as in the validation case of section 2.1 and the same computational scheme is employed.

To clearly show how C_1 behaves in all the experimental cases, figure 3 is plotted and indicates that C_1 decreases rapidly with the increase of bin ratio in the '1×' case. When the initial particle-number density increases, the decrease rate of C_1 is reduced. Therefore, using this model, the inner-collision effect can be pre-determined based on the bin-volume ratio and the particle-number density. However, the advantage of this model lies in the problems with large bin ratios where the inner-bin collision can be neglected.

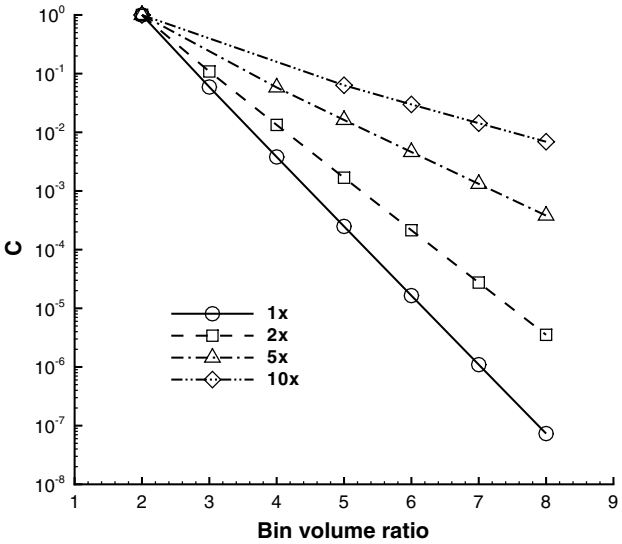

Figure 3. Variation of *C* versus the bin-volume ratio, with different initial particle-number densities of 1×, 2×, 5× and 10×.

3. Validation with measured data in a smoke-reduction experiment

Nanoparticle powders studied in this research are large nanoparticle aggregates of the size of tens of micrometres. When using injected nanoparticle powders to reduce the smoke in an indoor environment, a situation is created with a large number of particles having significantly different sizes. The injected nanoparticle aggregates (of the size of tens of micrometres) collide with the smoke particles (of the size of 2–3 micrometres) and stick to each other. Since the nanoparticle powders carrying the smoke particles have a much larger settling velocity than the original smoke particles, they will settle on the ground much faster and are therefore able to quickly remove the smoke particles from air.

Before the discussion of the flow and particulate phase equations used in this application, the collision kernel, $K_{i,j}$, used in the simulation needs to be defined. In the smoke-reduction application, the collision is induced by two effects: one is turbulence, the other is differential sedimentation. The turbulence collision kernel used here is again given by Saffman and Turner (1956), as expressed in equation (21). The differential-sedimentation-collision kernel is given by Williams (1988):

$$K_{(\mathrm{sed})\mathrm{i,j}} = \pi a_{i,j}^2 (U_{\mathrm{sett},i} - U_{\mathrm{sett},j}), \qquad \text{if } i > j, \tag{25}$$

where $U_{\mathrm{sett},i}$ is the settling speed for the particles of Size i. The differential sedimentation collision is induced by the difference in the settling speeds when larger particles with a faster settling speed catch the smaller particles with a slower settling speed in the path of the settling. Notice that the differential-sedimentation-collision effect is not significant when particle sizes are similar. It should be noted that the differential-sedimentation-collision kernel in equation (25) can possibly lead to fast unconstrained spreading of any nonstrictly monodisperse initial distribution. Williams (1988) noted that the actual collision frequency under the influence of gravity would be less than that indicated in equation (25) because the distortion of the velocity field by fluid affects the trajectories of approaching particles. To fix the problem, Williams (1988) defined collision efficiency as the ratio of the coagulation kernel with fluid effects to that without. In the current bin-volume collision model, unconstrained spreading of distributions would not occur because the model itself produces a well-behaved problem. In the smoke-reduction simulation application considered here, there are larger inertial effects than Brownian diffusion effects. With a relatively low turbulence level (except for the first few seconds) in the chamber, constant values of relative velocity can be assumed. Under these conditions, the collision efficiency is in the range 0.9–1 according to table 8 in Williams (1988). Therefore, the usage of equation (25) in this particular application can be justified.

Combining equations (21) and (25), the total collision kernel becomes

$$K_{i,j} = K_{(\mathrm{turb})i,j} + K_{(\mathrm{sed})i,j}. \tag{26}$$

The air/solid-particle flow problem is simulated by using an Euler-type formulation for both the air flow and the particulate phase. The continuous air-flow phase is governed by the unsteady compressible flow equations:

$$\frac{\partial \rho}{\partial t} + \vec{\nabla} \cdot (\rho \vec{u}) = 0 \tag{27}$$

and

$$\rho \frac{\mathrm{D}\vec{u}}{\mathrm{D}t} = -\vec{\nabla} p + \vec{\nabla} \cdot \bar{\bar{\tau}}, \tag{28}$$

where the body force, either due to the gravitational acceleration or arising from interactions with the solid particles, is neglected. It is therefore assumed that the air flow affects the particulate phase significantly, while the behaviour of the particulate phase does not have any effect on the air flow. This one-way interaction assumption is justified for the light-loading particulate phase considered here (Zhang *et al* 2005).

The collision model discussed in the previous sections is used to include the collision effect. Because of the large size difference between the injected particles and smoke particles in this study, the model with only inter-bin collisions is used. Another reason for neglecting the inner-bin collision is the collision kernel. For most of the smoke-reduction process, the differential-sedimentation-collision effect is dominant in the collision kernel. The particles within the same bin are similar in size, thus having similar settling speeds. As a result, the collision kernel, $K_{i,i}$, calculated from equation (25) between two similar sized particles is close to zero, and the second and fourth terms in equation (24) are negligible. Therefore, the inner-bin collision effect is minimal. Without the inner-bin collision, the particulate phase transport equation is

$$\frac{\partial n_i}{\partial t} + \vec{\nabla} \cdot (\vec{u} n_i) = -\vec{U}_{\mathrm{sett}} \cdot \vec{\nabla} n_i + \vec{\nabla} \cdot (D_{\mathrm{d}} \vec{\nabla} n_i) + \sum_{j=1}^{i-1} \frac{\gamma_i}{\gamma_j V_{i,j}} K_{i,j} n_i n_j - n_i \sum_{j=i+1}^{\infty} K_{i,j} n_j, \tag{29}$$

where D_{d} is the diffusivity (both laminar and turbulent) of the particles in air and $\vec{U}_{\mathrm{sett}}$ is the particle settling speed defined as

$$\vec{U}_{\mathrm{sett}} = C_{\mathrm{c}} \tau_{\mathrm{p}} \vec{g}. \tag{30}$$

In equation (30), C_{c} is the slip correction factor (Hinds 1982), $\vec{g}$ is the gravitational acceleration and τ_{p} is the particle settling time defined as

$$\tau_{\mathrm{p}} = \frac{\rho_{\mathrm{p}} d_{\mathrm{p}}^2}{18\mu}.$$

The diffusion coefficient in equation (29), D_{d}, combines the laminar and turbulent diffusion parts, D_{l} and D_{t}. The laminar diffusion coefficient is calculated using the Stoke–Einstein equation (Hinds 1982):

$$D_{\mathrm{l}} = \frac{kTC_{\mathrm{c}}}{3\pi \mu d_{\mathrm{p}}}, \tag{31}$$

where k is the Boltzmann constant, 1.38×10^{-23} (N m K^{-1}), T is the absolute temperature, C_{c} is the slip correction factor and μ is the dynamic viscosity of the flow. The turbulent diffusion coefficient is defined by

$$D_{\mathrm{t}} = \frac{\nu_{\mathrm{t}}}{Sc_{\mathrm{t}}}, \tag{32}$$

where ν_{t} is the turbulent viscosity and Sc_{t} is the turbulent Schmidt number. The turbulent Schmidt number measures the relative diffusion of momentum and mass due to turbulence and is on the order of unity in all turbulent flows. Because it is an empirical constant that is relatively insensitive to the molecular fluid properties, here it is set to be 0.7 (Yimer *et al* 2002) for all cases.

It needs to be pointed out that in obtaining equation (29), the small-slip continuum model (Zhou 1993) is applied, which is compatible with the one-way flow–particle interaction assumption. The boundary condition requirements in the particulate phase, for each of the convection, diffusion and settling effects, were studied previously (Zheng and Zhang

2005). The values of volume ratio, $V_{i,j}$, will be determined based on the application case in this section later.

In the solution procedure, the FLUENT flow solver with the realizable $k-\epsilon$ turbulence model (Shih *et al* 1994) is used to solve equations (27) and (28), because of the better behaviour of this model than a standard $k-\epsilon$ model for low Reynolds number flow. The computational scheme is second-order in time and space. The second-order upwind scheme is used for the convection terms, and the second-order central differencing is used for the diffusion terms.

Once the flow-field solutions are obtained, the velocity field is input to the particulate phase computing subroutines to solve equation (29). For solving the particulate phase transport equation, equation (29), a passive scalar transport equation solver in FLUENT is used with some modifications. For a passive scalar ϕ_i, a general convection–diffusion equation,

$$\frac{\partial \rho \phi_i}{\partial t} + \vec{\nabla} \cdot (\rho \vec{u} \phi_i) - \vec{\nabla} \cdot (\Gamma_i \vec{\nabla} \phi_i) = S_i \ (i = 1, \ldots, N) \quad (33)$$

can be solved in FLUENT using similar schemes in the flow solver, where Γ_i and S_i are the diffusion coefficient and source term that can be supplied by the user for each of the N scalar equations.

In order to make use of the solver for equation (33), equation (29) can be re-written as

$$\frac{\partial n_i}{\partial t} + \vec{\nabla} \cdot [(\vec{u} + \vec{U}_{\text{sett}}) n_i] - \vec{\nabla} \cdot (D_{\text{d}} \vec{\nabla} n_i) = \sum_{j=1}^{i-1} \frac{\gamma_i}{\gamma_j V_{i,j}} K_{i,j} n_i n_j - n_i \sum_{j=i+1}^{\infty} K_{i,j} n_j. \quad (34)$$

In this format, D_{d} is calculated as Γ_i in equation (33) with a user-defined function (UDF) called 'DEFINE_DIFFUSIVITY' to calculate the diffusion coefficient on every grid point of the computational domain. The diffusion terms are then discretized using the second-order central differencing. The collision terms, which are the right-hand side terms in equation (34), are implemented as the source term S_i using the UDF 'DEFINE_SOURCE.' The source term is handled explicitly.

On further comparing the format of equation (34) with that of equation (33), it can be seen that modifications are needed for the convection and unsteady terms. The convection and settling terms of equation (34) are combined as the convection term and solved implicitly. The convection term in its original scalar transport equation, equation (33), has the following general form:

$$\nabla \cdot \vec{\psi} \phi_i, \quad (35)$$

where $\vec{\psi}$ is a vector field. In the default convection term in equation (33), $\vec{\psi}$ is the product of the density and the velocity vector:

$$\vec{\psi}_{\text{default}} = \rho_{\text{f}} \vec{u}, \quad (36)$$

where ρ_{f} is the density on the cell face. Note that the $\vec{\psi}_{\text{default}}$ on all cell faces are automatically computed during the procedure in solving the flow in FLUENT and can be directly accessed by the user. To define the convection term using the UDF 'DEFINE_UDS_FLUX', the user needs to return the scalar value $\vec{\psi} \cdot \vec{A}$ to FLUENT, where $\vec{A}$ is the face normal vector of the cell face. $\vec{A}$ of all cell faces are calculated by FLUENT and can be accessed. Since there is no ρ in equation (34) and the settling term is added, the returned $\vec{\psi} \cdot \vec{A}$ becomes

$$\vec{\psi} \cdot \vec{A} = \vec{\psi}_{\text{default}} \cdot \vec{A} / \rho_{\text{f}} + \vec{U}_{\text{sett}} \cdot \vec{A}. \quad (37)$$

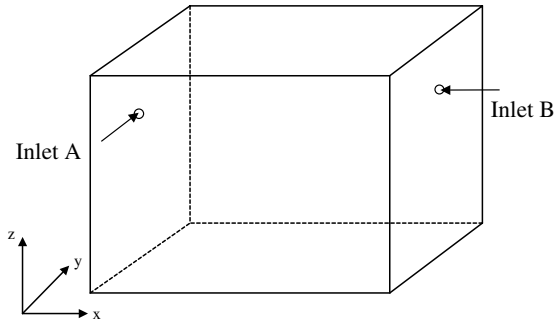

Figure 4. Illustration of the chamber and the particle injection ports and the coordinate system used in the simulation.

Because only the ρ value of the cell is recorded in the flow solver, the face value ρ_{f} is calculated as the average of two neighbouring cell values. The convection terms are discretized using the second-order upwind scheme.

Finally, for the unsteady term in the scalar transport equation, the only thing that needs to be modified is to re-define the coefficients of the unsteady term to remove the density in the default format. The solver requires that the unsteady term be decomposed into an implicit and an explicit component. For the finite-volume scheme with a first-order march in time, we have

$$\int \frac{\partial n_i}{\partial t} \mathrm{d}V = \frac{\Delta V}{\Delta t} n_i^m - \frac{\Delta V}{\Delta t} n_i^{m-1}, \quad (38)$$

where ΔV represents the volume of the cell and m represents the current time step. In the UDF 'DEFINE_UDS_UNSTEADY,' the coefficient of the implicit term (the n_i^m term) and the whole explicit term are the two variables to be input to the solver. Therefore, the above computational scheme of the particulate phase using equation (29) or (34) is first-order accurate in time and second-order accurate in space.

Figure 4 illustrates the chamber geometry in the experiment and simulation whose spatial dimensions are 3.7 m × 2.4 m × 2.4 m in the x, y and z directions, respectively. A 96 × 64 × 64 grid mesh is placed in the three-dimensional computational domain. Higher and lower resolution grids were also tested to determine the necessary resolution for grid-independent simulations. The particles are deployed through one of the inlet ports with a velocity of 40 m s^{-1}. The injection lasts 2 s. The location of the inlet port A is at the upper left quadrant 0.6 m from the left-end wall ($x = 0.6$) and 0.4 m from the ceiling ($z = 2.0$); the inlet port B is located at the right-end wall ($x = 3.7$) and at the centre of the wall ($y = 1.2$) and 0.57 m from the ceiling ($z = 1.83$). Detailed descriptions of the injection and measurement setup are presented in Zhang *et al* (2005). The validations of the particle deposition and the spatial distribution showed good agreement with the measured data (Zhang *et al* 2005).

As illustrated in figure 4, the injection of nanoparticle powders was through inlet port A and lasted 2 s. Initially the chamber was filled with glycol smoke uniformly, and the mass concentration was 150 mg m^{-3}, with a total mass of 3.26 g. The size of the smoke particle was approximately 2.5 μm, and the material density of smoke particles was 1 g cm^{-3}. The total mass of MgO+ nanoparticles (NanoScale Material

Table 2. Volume ratios between particles of two bins (v_i/v_j).

$j\backslash i$	2.5 μm	10 μm	20 μm	40 μm	90 μm
2.5 μm	1	64	512	4096	46656
10 μm	1/64	1	8	64	729
20 μm	1/512	1/8	1	8	91.13
40 μm	1/4096	1/64	1/8	1	11.39
90 μm	1/46656	1/729	1/91.13	1/11.39	1

Table 3. Injected particle properties and inlet boundary conditions.

Bin size (μm)	Mass (g)	Inlet n (count/m^3)	Settling velocity (m s^{-1})
10(<15)	5	2.0E+11	0.001 214
20(15–30)	12	6.0E+10	0.004 856
40(30–60)	15	9.4E+09	0.019 424
90(>60)	20	1.1E+09	0.098 334

Inc.) injected into the chamber was 52.3 g. The size of injected particles ranges from 5 to 140 μm. The total mass concentration combining smoke and injected particles at the centre of the chamber was recorded using a tapered element oscillating microbalance (TEOM). In the simulation, five bins of particles are allocated to represent the smoke and injected particles and they are 2.5 μm (smoke), 10, 20, 40 and 90 μm. The volume ratios between the five bins, calculated using equation (5), are listed in table 2.

Since there is no particle-size-distribution measurement at the inlet, there is no measured inlet particle-number density to be used for the inlet boundary condition for simulation. One way to find the approximate mass percentage of particles in each bin from the total 52.3 g injected mass is to compare with the deposition measurement data (Zhang *et al* 2005). We counted the total number of particles of each size range in the whole experimental period, and then calculated the mass ratios among different size ranges. Table 3 shows the mass for each bin's particles and the corresponding inlet particle-number density.

Figure 5 shows the comparison of the time history of the total mass concentration of all sizes of particles at the centre of the chamber. Because of the uncertainty in the inlet boundary condition, an exact match between the simulation result and experimental measurement is not expected. In figure 5, the simulation results overpredict the mass concentration at the first point (1 min). After that, the agreement with the experimental data is relatively good. In both the simulation result and experimental data, the decaying trend of the total mass concentration can be clearly identified. Both the curves become flat after about 10 min. This is because after 10 min only a small number of injected particles is left in the chamber. At the end of 20 min, the simulation result tends to overpredict the mass concentration a little compared with the experimental data. Finally, figure 5 also shows that the mass concentrations from both the results are not less than the initial mass concentration even after 20 min. The final mass concentration includes both the injected particles and smoke particles. In spite of the fact that smoke particles have been reduced (shown in figure 6), the measure of effectiveness of clearing the chamber should include the total mass concentration of both the injected particles and smoke particles remaining in the

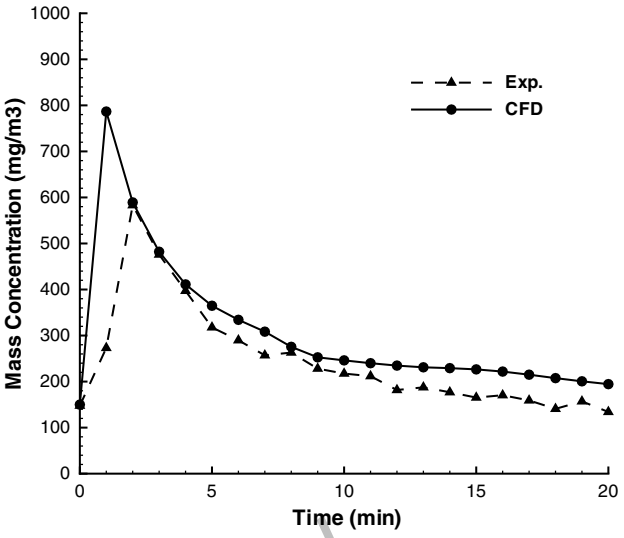

Figure 5. Time history comparison of total mass concentration at the centre of the chamber with the experimental measurement.

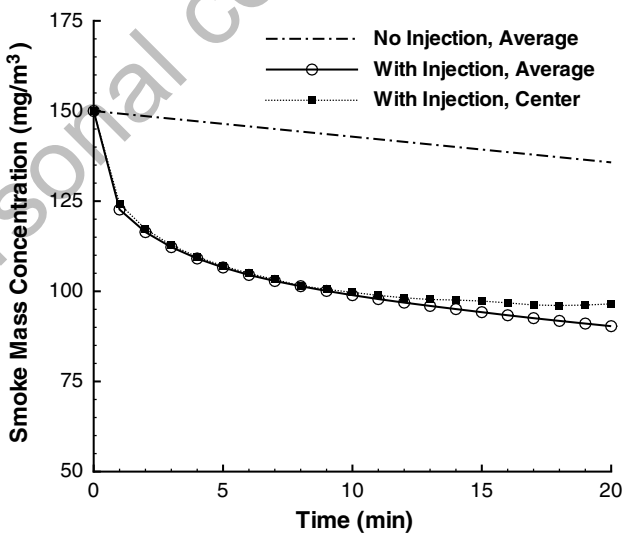

Figure 6. Simulated time histories of mass concentration of smoke particles in the chamber.

chamber. Therefore the results in figure 5 indicate that this injection configuration is not very effective in smoke clearance. In addition to the particle properties, the ineffectiveness could also be attributed to the injection method used in the case (Zhang *et al* 2005), a factor on which further investigations are needed.

Because the experiment was not able to measure the mass concentration of smoke particles separately, figure 6 is used to analyse the result for smoke particles based only on the simulation. In figure 6, the no injection curve represents the history of average smoke mass concentration throughout the chamber in the case of no particle injection (and also no flow in the chamber). The reduction of smoke in the no injection situation is only caused by the gravitational settling of smoke particles. There is about a 9% reduction after 20 min. For the case with injection, one curve is the history of average smoke mass concentration throughout the chamber and the

other is the history of the local smoke mass concentration at the centre of the chamber. The average mass concentration indicates the amount of smoke left in the chamber, and is a better representation of the effect of smoke reduction in the whole chamber. There is about a 40% reduction after 20 min with the injection. This shows that the injection of nanoparticles significantly enhances the reduction of smoke particles, although not necessarily the overall clearance of the chamber as indicated in figure 5. The curve of mass concentration at the chamber centre is very close to the average mass concentration curve, which justifies the use of the value measured at the chamber centre to represent the mass concentration in the whole chamber for comparisons in figure 5. The mass concentration at the centre is a little higher than the average value at the end of the 20 min period. It is noticed that the curve for the injection case becomes parallel to the no injection curve after about 10 min, indicating that there are not many injected particles left after 10 min and that the reduction rate is mostly due to the smoke particle settling.

By comparing the simulation results after the 10 min period in figures 5 and 6, nanoparticles and smoke particles each contribute approximately half of the mass concentration (each about 100 mg m^{-3}) in the chamber. Since the injected nanoparticles have much larger sizes than the smoke particles, the number of nanoparticles is much smaller than that of smoke particles. Therefore there is little smoke-reduction capability left after 10 min, resulting in the parallel curves in figure 6 between the cases with and without injection. The simulation result tends to underpredict the particle reduction rate in comparison with the measurement data, partly because the inner-bin collisions are neglected. The overpredicted total mass concentration at the end of 20 min of the simulation result above that of the measurement in figure 5, about 50 mg m^{-3}, should be attributed to both smoke particles and nanoparticles.

4. Conclusions

A collision model based on mass balance among the bin structures is developed and successfully validated against the exact solution. The model fits best when the bin-volume ratio is large and the inner-bin collision can be neglected. For smaller bin ratios, an inner-bin-collision coefficient needs to be considered to include the inner-bin-collision effect. This coefficient decreases when the bin ratio increases. The decrease is more rapid when the particle-number density in a bin is smaller. Using this collision model, the computational overhead of the simulation can be reduced significantly. The model is implemented with a flow solver to simulate a smoke-reduction experiment using the injection of nanoparticles. The simulation results are compared with the experimental measurement data, and the good agreement provides further evidence of the validity of the present collision model. The collision model effectively represents a significant enhancement in removing smoke particles with injected nanoparticles.

Acknowledgments

This work was partially funded through the award of a contract from the United States Marine Corps Systems Command to M2 Technologies, Inc.

References

Batterham R J, Hall J S and Barton G 1981 Pelletizing kinetics and simulation of full scale balling circuits *Proc. 3rd Int. Symp. Agglomeration (Nurnberg, Federal Republic of Germany)*

Fernandez-Diaz J M, Muniz C G, Brana M A R, Garcia B A and Nieto P J G 2000 A modified semi-implicit method to obtain the evolution of an aerosol by coagulation *Atmos. Environ.* **34** 4301–14

Gelbard F, Tambour Y and Seinfeld J H 1980 Sectional representations for simulating aerosol dynamics *J. Colloid Interface Sci.* **76** 541–56

Hinds W C 1982 *Aerosol Technol.* (New York: Wiley)

Hounslow M J, Ryall R L and Marshall V R 1988 Discretized population balance for nucleation, growth, and aggregation *AIChE J.* **34** 1821–32

Jacobson M Z, Turco R P, Jensen E J and Toon O B 1994 Modeling coagulation among particles of different composition and size *Atmos. Environ.* **28** 1327–38

Kostoglou M and Karabelas 1994 Evaluation of zero order methods for simulating particle coagulation *J. Colloid Interface Sci.* **163** 420–31

Kostoglou M, Konstandopoulos A G and Friedlander S K 2006 Bivariate population dynamics simulation of fractal aerosol aggregate coagulation and restructuring *Aerosol Sci.* **37** 1102–15

Lawler D F, O'Melia C R and Tobiason J E 1980 Particulates in Water (Washington, DC: American Chemical Society) pp 353–90

Marchal P, David R, Klein J P and Villermaux 1988 Crystallization and precipitation engineering: I. An efficient method for solving population balance in crystallization with agglomeration *J. Chem. Eng. Sci.* **43** 59–67

Reade W C and Collins L R 2000 A numerical study of the particle size distribution of an aerosol undergoing turbulence coagulation *J. Fluid Mech.* **415** 45–64

Saffman P G and Turner J S 1956 On the collision of drops in turbulent clouds *J. Fluid Mech.* **1** 16–30

Sandu A 2002 A Newton–Cotes quadrature approach for solving the aerosol coagulation equation *Atmos. Environ.* **36** 583–98

Shih T H, Liou W W, Shabbir A, Yang Z and Zhu J 1994 A new $k-\epsilon$ eddy viscosity model for high Reynolds number turbulent flows *Comput. Fluids* **24** 227–38

Smoluchowski M 1917 Versuch einer mathematischen theorie der koagulationskinetic kolloider losungen *Z. Phys. Chem.* **92** 129

Williams M M R 1988 A unified theory of aerosol coagulation *J. Phys. D: Appl. Phys.* **21** 875–86

Yimer I, Campbell I and Jiang L-Y 2002 Estimation of the turbulent Schmidt number from experimental profiles of axial velocity and concentration for high-Reynolds-number jet flows *Can. Aeronaut. Space J.* **48** 195–200

Zhang N, Zheng Z C, Glasgow L and Braley B 2005 Particle deposition in a room-sized chamber with particle injection *Proc. 2005 ASME Fluid and Engineering Division Summer Conf. (Houston, Texas, USA)*

Zheng Z C and Zhang N 2005 Integral characteristics of mass conservation of particles in flow *Proc. 4th AIAA Theoretical Fluid Mechanics Meeting (Toronto, Canada)*

Zhou L 1993 *Theory and Numerical Modeling of Turbulent Gas-Particle Flows and Combustion* (Beijing: Science Press/Boca Raton, FL: CRC Press)